ELSEVIER

Journal of Alloys and Compounds 349 (2003) 28–36

Journal of ALLOYS AND COMPOUNDS

www.elsevier.com/locate/jallcom

Lattice dynamics of YCu_2

K. Hense[a], E. Gratz[a,*], A. Lindbaum[a], H. Michor[a], H. Nowotny[b], F. Güthoff[c,d], A. Hoser[c,d], P. Knoll[e]

[a]*Institute for Solid State Physics, Vienna University of Technology, Wiedner Hauptstraße 8–10, A-1040 Wien, Austria*
[b]*Institute for Theoretical Physics, Vienna University of Technology, Vienna, Austria*
[c]*Institut für Kristallographie, RWTH Aachen, Jägerstraße 17–19, D-52066 Aachen, Germany*
[d]*IFF, Forschungszentrum Juelich, Juelich, Germany*
[e]*Institute for Experimental Physics, University Graz, Universitätsplatz 5, A-8010 Graz, Austria*

Received 19 June 2002; received in revised form 3 July 2002; accepted 3 July 2002

Abstract

The lattice dynamics of the orthorhombic YCu_2 compound has been studied by inelastic neutron scattering on a single crystal. An axially symmetric Born–von Karman model was applied to fit the neutron data. Ab initio calculations of the lattice dynamics at the Γ-point provided important additional information for the Born–von Karman fit procedure. The calculated phonon density of states was compared with time-of-flight experiments on powdered YCu_2 sample material. The experimental studies were completed by Raman experiments and measurements of specific heat, thermal expansion, and compressibility.

Keywords: Rare earth compounds; Phonons; Neutron scattering; Heat capacity

1. Introduction

The intermetallic RT_2 compounds with R = rare earth and T = transition metals (Mn, Fe, Co, and Ni) or Al crystallize in the cubic Laves phase type structure (space group *Fd3m*), with a few exceptions in the RMn_2 series (R = Dy, Ho, Er, Tm) which crystallize in the hexagonal Laves phase type structure. The physical properties of these Laves phase compounds have been studied in the last four decades in many details, mainly because of the large variety of magnetic phenomena for which these intermetallics are known [1]. When proceeding in the periodic table, the compounds with Cu do not show the Laves phase structure, but crystallize in the orthorhombic $CeCu_2$-type structure (space group *Imma*). Recently a number of investigations have been published concerning the properties of the RCu_2 series. Mainly investigations of the magnetic properties, such as magnetic phase diagram studies have been done [2,3].

In contrast to the cubic 1:2 intermetallics, a systematic study of the lattice dynamics for the low symmetric orthorhombic 1:2 compounds does not exist, at least to our knowledge.

A rough estimation whether there is a change in the lattice dynamics (when the structure transforms from cubic to orthorhombic) can be gained from a comparison of the Debye temperatures of both structure types. For this purpose the Debye temperature Θ_D for two nonmagnetic representatives selected from both series are compared: YAl_2, $\Theta_D = 330$ K (from resistivity measurements) [4] and 322 K (from thermal expansion measurements) [5]; YCu_2, $\Theta_D = 170$ K (from resistivity measurements) [6] and 197 K (from thermal expansion measurements—see Section 4.4). The considerably smaller Θ_D value of YCu_2 can be interpreted as a sign for the 'softer' lattice of the compound crystallizing in the orthorhombic structure.

However, a real measure of the lattice dynamics can only be obtained by inelastic neutron scattering experiments on a single crystal. The study of the lattice dynamics in YCu_2 is important in order to shed more light on the phonon system of such a rather low symmetric system. Furthermore a detailed knowledge of the phonon dispersion relation is a necessary spadework for a future study of the crystal field–phonon interaction in the isostructural $NdCu_2$.

*Corresponding author. Fax: +43-1-58801-13199.
E-mail address: ernst.gratz@ifp.tuwien.ac.at (E. Gratz).

0925-8388/02/$ – see front matter
PII: S0925-8388(02)00916-7

The goal of this publication can be summarized as follows:

1. presentation of the phonon dispersion relation of YCu_2, where the experimental data are fitted using a Born–von Karman model;
2. comparison of these results with experiments such as Raman spectroscopy, specific heat, elastic constants, thermal expansion and compressibility measurements.

2. Sample preparation and experimental details

2.1. Sample preparation

A polycrystalline ingot of YCu_2 was prepared by melting appropriate quantities of highly purified starting materials in an induction furnace under a protective argon atmosphere. Single crystals were grown from this material using the Bridgman technique. For the crucible material BN was used, with argon as protective gas during the growing procedure. The quantity of the polycrystalline starting material for the growing procedure was about 20 g. With this method we were able to prepare a single crystal with a volume of about 0.45 cm^3. The crystal was oriented by the X-ray Laue technique.

2.2. Neutron diffraction experiments

The single crystal measurements for determining the phonon dispersion relation were performed using the UNIDAS triple axis spectrometer at the DIDO reactor in the Research Centre Juelich [7]. For the low energy part of the acoustic phonons constant energy scans were made, otherwise constant Q-scans. For the low-lying optical phonon branches $k_i = 2.66$ Å^{-1} was used, for the higher optical phonon branches $k_i = 3.62$ Å^{-1} has been chosen. The quality of the crystal was checked by measuring the Rocking curves on the (200) and (002) Bragg reflections. A weak shoulder on the flank of the (200) peak has been found which is obviously caused by a twinning of a small part in the sample material, whereas the Rocking curve on the (002) Bragg reflection was ideal.

For the measurement of the phonon density of states (PDOS) a time-of-flight experiment was performed on a polycrystalline sample of YCu_2 (55 g) using the LRMECS at IPNS Argonne National Laboratory. The LRMECS spectrometer is equipped with a wide-angle multidetector bank. The incident neutron energy of 35 meV allows measurements of inelastic scattering over a relatively wide range of momentum and energy transfer with reasonable energy resolution [8]. The powder was contained in a planar aluminum sample holder mounted at a 45° angle to the incident neutron beam. Such a geometry decreases the neutron traverse length in the sample to about 5 mm for all the detector angles—thereby reducing multiple scattering effects. Multiple scattering was estimated to be less than 5% of the total measured intensity. To reduce multiple-phonon excitations the sample was kept at 15 K for the experiment. Normal background scattering was subtracted from the data by performing empty-container runs. Measurements of elastic incoherent scattering from a vanadium standard provided detector calibration and intensity normalization.

2.3. Other experiments

Micro Raman measurements have been performed on the single crystal at room temperature and at liquid nitrogen temperature using the scanning multichannel technology [9]. We used several excitations of an Ar- and Kr-Laser and detected the Raman signal with a triple spectrometer and an attached liquid nitrogen cooled CCD detector. The laser power was kept low enough to avoid sample damage at the different temperatures. From the different polarization geometries the Γ-point phonon frequencies have been determined for the different symmetries.

Specific heat measurements in the temperature range from 4.2 up to 100 K were carried out in a quasi-adiabatic calorimeter employing a modified Nernst step-heating technique. For the thermal expansion measurement a X-ray diffractometer equipped with a He-flow cryostat has been used. The compressibility of YCu_2 has been measured at the X-ray diffraction beamline of the ELETTRA synchrotron source (Trieste, Italy) using a diamond anvil cell (DAC) [10].

3. Data analysis

3.1. Crystal structure and normal mode analysis

In the RCu_2 series (D_{2h}^{28}; *Imma* space group), the R atoms occupy the Wyckoff 4(*e*) sites (C_{2v}^{z}; *mm2* symmetry) and the Cu atoms occupy the 8(*h*) sites (C_s^{yz}; *m* symmetry). The arrangement of the atoms in the unit cell is shown in Fig. 1 and the structural parameters are given in Table 1. There are three atomic position parameters which are not fixed by the space group symmetry. As the primitive cell contains six atoms, one expects 18 phonon branches, which show no degeneracy along the three main symmetry directions. Nine of these branches are found to be Raman active at the Γ-point [11]. From group theoretical considerations one can find a decomposition of the phonon branches at the Γ-point and at the symmetry lines as given in Table 2.

Since there are only eight symmetry elements in the point group, one has to consider 1/8 of the first Brillouin zone (BZ) (in contrast to the full cubic symmetry of the C15 structure, where only 1/48 has to be considered). The measurements of the phonon dispersion were performed

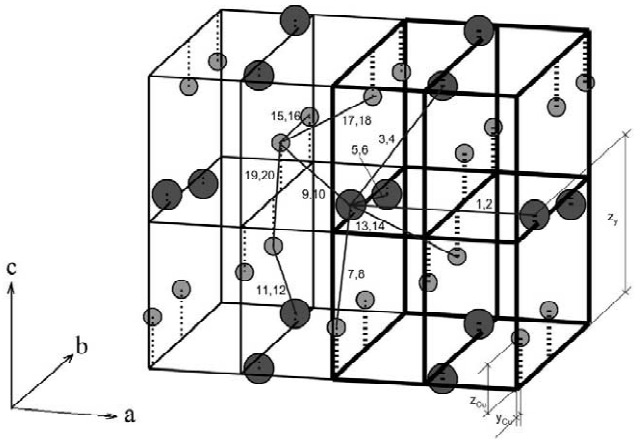

Fig. 1. The atomic arrangement in two adjacent orthorhombic unit cells of YCu_2 is shown. The large symbols indicate the Y atoms and the small the Cu atoms. The lines and the numbers correspond to the springs and the force constants given in Table 8.

Table 1
The structural parameters for YCu_2

Atom no.	Atom type	Cartesian coordinates		
1	Y_1	0	1/4	z_Y
2	Y_2	0	$-1/4$	$-z_Y$
3	Cu_1	0	y_{Cu}	z_{Cu}
4	Cu_2	0	$-y_{Cu}$	$-z_{Cu}$
5	Cu_3	0	$-1/2+y_{Cu}$	$-z_{Cu}$
6	Cu_4	0	$1/2-y_{Cu}$	z_{Cu}
		+ (1/2, 1/2, 1/2)		

The space group for this structure is *Imma* (No. 74), $a=4.305$ Å, $b=6.872$ Å, $c=7.295$ Å. Y atoms occupy the 4(*e*) sites, Cu atoms the 8(*h*) sites. The yttrium fractional position parameter is $z_Y=0.544$, the copper fractional position parameters are $y_{Cu}=0.050$, $z_{Cu}=0.162$.

mainly along the high symmetry directions Σ, Δ and Λ which are parallel to the *a**-, *b**-, and *c**-direction of the reciprocal unit cell and show C_{2v} symmetry. The shape of the first BZ and a cut in the (*a**, *b**)-plane of the reciprocal space is shown in Fig. 2.

When leaving the Γ-point (D_{2h} symmetry) along the symmetry lines (C_{2v} symmetry), the number of symmetry elements is reduced from 8 to 4. Therefore, the number of irreducible representations decreases also from 8 to 4 (the corresponding character tables are given in Tables 3 and 4). Comparing the character tables given by Burns [11], one can find the compatibility relations of the branches

Table 2
Symmetry decomposition of the phonon branches for the Γ-point and the high-symmetry lines

Symmetry point:			Decomposition
Γ(mmm)	D_{2h}	(000)	$3\Gamma_1+1\Gamma_2+3\Gamma_3+2\Gamma_4+2\Gamma_5+3\Gamma_6+1\Gamma_7+3\Gamma_8$
Symmetry lines:			Decomposition
Σ(mm2)	C_{2v}	[ζ00]	$5\Sigma_1+4\Sigma_2+5\Sigma_3+4\Sigma_4$
Δ(mm2)	C_{2v}	[0ζ0]	$6\Delta_1+3\Delta_2+6\Delta_3+3\Delta_4$
Λ(mm2)	C_{2v}	[00ζ]	$6\Lambda_1+2\Lambda_2+6\Lambda_3+4\Lambda_4$

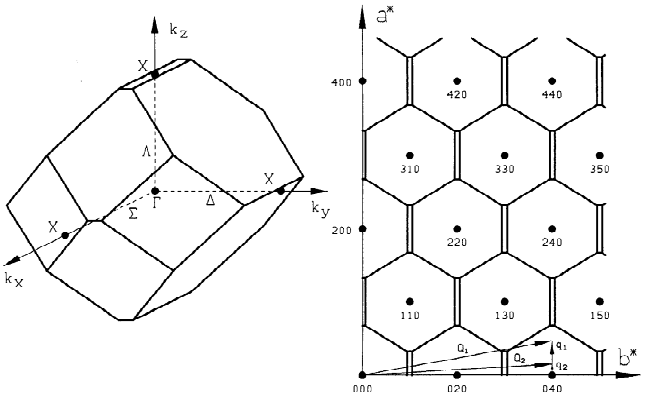

Fig. 2. The shape of the Brillouin zone of the orthorhombic $CeCu_2$-type structure (space group: *Imma*) and a cut of the extended zone schema in the (*a**, *b**) plane. The numbers characterize reciprocal lattice vectors. The vectors $\vec{Q}_1$ and $\vec{Q}_2$ in the (*a**, *b**)-plane indicate the position where the constant *Q*-scans where performed which are shown as an example in Fig. 3.

Table 3
Irreducible representations of the group mmm (D_{2h})

D_{2h}	mmm	E	C_2^x	C_2^y	C_2^z	I	σ_x	σ_y	σ_z
A_g	Γ_1	1	1	1	1	1	1	1	1
A_u	Γ_2	1	1	1	1	−1	−1	−1	−1
B_{3g}	Γ_3	1	1	−1	−1	1	1	−1	1
B_{3u}	Γ_4	1	1	−1	−1	−1	−1	1	1
B_{2g}	Γ_5	1	−1	1	−1	1	−1	1	−1
B_{2u}	Γ_6	1	−1	1	−1	−1	1	−1	1
B_{1g}	Γ_7	1	−1	−1	1	1	−1	−1	1
B_{1u}	Γ_8	1	−1	−1	1	−1	1	1	−1

The first column is according to Burns [11], the second column is according to the output of UNISOFT [12].

given in Table 5. The representations are labeled according to the name of the symmetry-point or -direction to which they belong. The enumeration is chosen according to UNISOFT [12]. Using only symmetry considerations one is able to calculate the symmetry of the displacement-vector for each phonon at the Γ-point. The 18 components of each displacement vector are given in Table 6 (for Raman active phonons) and Table 7 (for Raman inactive phonons) by the cartesian coordinates for each of the six different atoms in the primitive unit cell (Y_1, Y_2, Cu_1, Cu_2, Cu_3, Cu_4). Capital letters (*A*, *B*) and small letters (*a*, *b*) indicate big and small values of the normalized dis-

Table 4
Irreducible representations of the group mm2 (C_{2v}) according to the output of UNISOFT [12]

Σ(mm2)			E	C_2^x	σ_y	σ_z
	Δ(mm2)		E	C_2^y	σ_x	σ_z
		Λ(mm2)	E	C_2^z	σ_x	σ_y
Σ_1	Δ_1	Λ_1	1	1	1	1
Σ_2	Δ_2	Λ_2	1	1	−1	−1
Σ_3	Δ_3	Λ_3	1	−1	1	−1
Σ_4	Δ_4	Λ_4	1	−1	−1	1

Table 5
Compatibility relations between the Γ-point and the high symmetry lines

Γ-point	Σ-line [ζ00]	Δ-line [0ζ0]	Λ-line [00ζ]
Γ_1	Σ_1	Δ_1	Λ_1
Γ_2	Σ_2	Δ_2	Λ_2
Γ_3	Σ_2	Δ_3	Λ_3
Γ_4	Σ_1	Δ_4	Λ_4
Γ_5	Σ_3	Δ_2	Λ_4
Γ_6	Σ_4	Δ_1	Λ_3
Γ_7	Σ_4	Δ_4	Λ_2
Γ_8	Σ_3	Δ_3	Λ_1

placement vectors. For one phonon the same letter indicates the same magnitude. However, for different phonons *A*, *B*, *a*, *b* will in general have different numerical values.

The values of *A*, *a*, *B* and *b* are positive, a negative displacement is given explicitly by the minus sign. Tables 6 and 7 show that phonons at the Γ-point consist of atomic displacements either only in the *a*-direction or in the *b*–*c* plane. The tables are arranged according to increasing phonon energy obtained from the Born–von Karman model calculation (see Section 3.2).

3.2. Born–von Karman fit procedure

In measuring the phonons of YCu_2 most difficulties arise owing to the relatively large number of optical phonon branches in a quite narrow energy range (less than 4 THz). In order to give an example for measured phonons two constant *Q*-scans at $\vec{Q}_1 = (0.47,4,0)$ (transversal acoustic phonon) and at $\vec{Q}_2 = (0.15,4,0)$ (optical phonons) are shown in Fig. 3. In the low symmetric orthorhombic YCu_2 compound none of the 18 phonon branches are identical (degenerate) along the high symmetry directions Σ, Δ and Λ.

It is very difficult to start the Born–von Karman fit procedure without additional information. Therefore constant *Q*-scans at the Γ-point in various Brillouin zones in the extended zone schema have been performed. In order to determine the polarization of the observed phonons the relative intensities were compared with calculated dynamical structure factors. Furthermore all observed Γ-point phonons were studied with increasing *Q*-values inside the Brillouin zone. Another source of information resulted from ab initio calculations at the Γ-point (see Section 3.3). Because of the good agreement between the ab initio calculations and the experiment, concerning the eigenfrequencies, it can be assumed that also the ab initio eigenvectors are correct and can be used as input for the iterative fit procedure of the force constants in the Born–von Karman model. This means that not only the experimentally determined eigenfrequencies of the phonon branches were taken as input, but also the ab initio results for the eigenvectors of the Γ-point phonons. In the axially

Table 6
Γ-point: amplitudes of Raman active phonons

Γ-point symmetry		$E = \hbar\omega$ [THz]	Amplitude Y_1	Y_2	Cu_1	Cu_2	Cu_3	Cu_4
A_g	Γ_1	2.44	$\begin{pmatrix} 0 & 0 & 0 & 0 & 0 & 0 \\ 0 & 0 & B & -B & B & -B \\ A & -A & -b & b & b & -b \end{pmatrix}$					
B_{3g}	Γ_3	2.79	$\begin{pmatrix} 0 & 0 & 0 & 0 & 0 & 0 \\ A & -A & -B & B & B & -B \\ 0 & 0 & b & -b & b & -b \end{pmatrix}$					
B_{1g}	Γ_7	2.95	$\begin{pmatrix} 0 & 0 & B & -B & B & -B \\ 0 & 0 & 0 & 0 & 0 & 0 \\ 0 & 0 & 0 & 0 & 0 & 0 \end{pmatrix}$					
B_{2g}	Γ_5	3.45	$\begin{pmatrix} A & -A & -b & b & b & -b \\ 0 & 0 & 0 & 0 & 0 & 0 \\ 0 & 0 & 0 & 0 & 0 & 0 \end{pmatrix}$					
B_{3g}	Γ_3	3.92	$\begin{pmatrix} 0 & 0 & 0 & 0 & 0 & 0 \\ -A & A & -b & b & b & -b \\ 0 & 0 & -B & B & -B & B \end{pmatrix}$					
A_g	Γ_1	4.80	$\begin{pmatrix} 0 & 0 & 0 & 0 & 0 & 0 \\ 0 & 0 & B & -B & B & -B \\ -A & A & b & -b & -b & b \end{pmatrix}$					
A_g	Γ_1	5.56	$\begin{pmatrix} 0 & 0 & 0 & 0 & 0 & 0 \\ 0 & 0 & b & -b & b & -b \\ A & -A & B & -B & -B & B \end{pmatrix}$					
B_{3g}	Γ_3	5.79	$\begin{pmatrix} 0 & 0 & 0 & 0 & 0 & 0 \\ -A & A & b & -b & -b & b \\ 0 & 0 & B & -B & B & -B \end{pmatrix}$					
B_{2g}	Γ_5	5.96	$\begin{pmatrix} a & -a & B & -B & -B & B \\ 0 & 0 & 0 & 0 & 0 & 0 \\ 0 & 0 & 0 & 0 & 0 & 0 \end{pmatrix}$					

Table 7
Γ-point: amplitudes of Raman inactive phonons

Γ-point symmetry		$E = \hbar\omega$ [THz]	Amplitude Y_1	Y_2	Cu_1	Cu_2	Cu_3	Cu_4
B_{3u}	Γ_4	0.00	$\begin{pmatrix} A & A & B & B & B & B \\ 0 & 0 & 0 & 0 & 0 & 0 \\ 0 & 0 & 0 & 0 & 0 & 0 \end{pmatrix}$					
B_{2u}	Γ_6	0.00	$\begin{pmatrix} 0 & 0 & 0 & 0 & 0 & 0 \\ A & A & B & B & B & B \\ 0 & 0 & 0 & 0 & 0 & 0 \end{pmatrix}$					
B_{1u}	Γ_8	0.00	$\begin{pmatrix} 0 & 0 & 0 & 0 & 0 & 0 \\ 0 & 0 & 0 & 0 & 0 & 0 \\ A & A & B & B & B & B \end{pmatrix}$					
B_{1u}	Γ_8	3.39	$\begin{pmatrix} 0 & 0 & 0 & 0 & 0 & 0 \\ 0 & 0 & B & B & -B & -B \\ -A & -A & b & b & b & b \end{pmatrix}$					
B_{2u}	Γ_6	3.76	$\begin{pmatrix} 0 & 0 & 0 & 0 & 0 & 0 \\ a & a & -b & -b & -b & -b \\ 0 & 0 & -B & -B & B & B \end{pmatrix}$					
B_{1u}	Γ_8	4.39	$\begin{pmatrix} 0 & 0 & 0 & 0 & 0 & 0 \\ 0 & 0 & B & B & -B & -B \\ A & A & -b & -b & -b & -b \end{pmatrix}$					
B_{3u}	Γ_4	4.44	$\begin{pmatrix} A & A & -B & -B & -B & -B \\ 0 & 0 & 0 & 0 & 0 & 0 \\ 0 & 0 & 0 & 0 & 0 & 0 \end{pmatrix}$					
B_{2u}	Γ_6	4.68	$\begin{pmatrix} 0 & 0 & 0 & 0 & 0 & 0 \\ -A & -A & b & b & b & b \\ 0 & 0 & -B & -B & B & B \end{pmatrix}$					
A_u	Γ_2	6.00	$\begin{pmatrix} 0 & 0 & B & B & -B & -B \\ 0 & 0 & 0 & 0 & 0 & 0 \\ 0 & 0 & 0 & 0 & 0 & 0 \end{pmatrix}$					

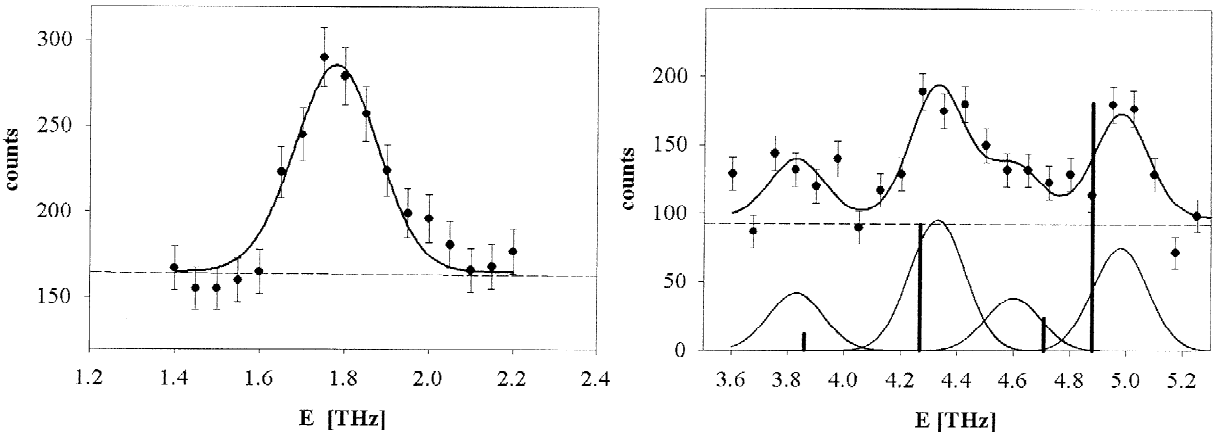

Fig. 3. Representative constant Q-scans are shown. Left: acoustic phonon measured at $\vec{Q}_1=(0.47,4,0)$. Right: optical phonons measured in the energy range from 3.6 to 5.3 THz at $\vec{Q}_2=(0.15,4,0)$. The solid lines in both graphs show the fit of the experimental data assuming Gaussian line shape. The broken line indicates the background position. The vertical lines give the position and intensities of the Born–von Karman model calculation.

symmetric Born–von Karman model, used for the fit of the neutron data, one assumes one radial (longitudinal) and only one transverse force constant between a pair of atoms [13]. The minimal number of springs needed for a successful fit was found to be 10, their maximum length is 4.31 Å (nearest Y_1–Y_1 distance along the a-axis). When reducing the number of springs, the dispersion relation cannot be described properly. Although the Born–von Karman model is simple, it has often been successfully used for fitting experimental phonon data of similar intermetallic compounds [14,15].

In Fig. 4 the calculated phonon dispersion relations (full and broken lines) for the three high symmetry directions are plotted. For the calculation of the dispersion curves the UNISOFT program was used [12]. The open circles in Fig. 4 indicate the neutron data as obtained with the UNIDAS triple axis spectrometer. The broken lines show which of the phonon branches are Raman active at the Γ-point. The data of the Raman measurements are given by full squares in Fig. 4. The agreement between these Raman data and the calculated Raman-active phonons can be seen at the Γ-point between the [00ζ] and [0ζ0] diagrams in Fig. 4. Another set of data is given by full circles at the Γ-point in the [ζ00] diagrams. These data are the results of the ab initio calculations. The overall agreement of the neutron data, the Raman data and the ab initio calculation at the Γ-point is good.

The differences between experiment and calculation are most important for the acoustic phonon branch with polarization in b-direction and propagation in [ζ00]-direction (see Fig. 4d). A careful estimation shows that this disagreement on the calculated phonon density of states (used for the calculation of the specific heat, see below) is negligible. It seems that the poor agreement concerning some of the transversal acoustic phonon branches (see Fig. 4) cannot be improved in the scope of the axially symmetric Born–von Karman model.

A comparison of the springs given in Table 8 shows that, except for the Cu–Cu interaction, the force constants decrease with increasing interatomic distances within one bonding type (e.g., bonding between Y and Y). The arrangement of the springs in the orthorhombic unit cell doubled along the a-axis is shown in Fig. 1. The numbers there identify the corresponding force constants.

3.3. Ab initio calculation of the phonons at the Γ-point

Ab initio calculations of the phonons at the Γ-point via the so-called force constant method based on electronic band-structure calculations were performed using the Vienna ab initio simulation package VASP [16–18]. For calculating the phonons at the Γ-point it is possible to choose the primitive unit cell as a 'supercell' in order to obtain results which are exact in the sense of frozen phonons. The primitive unit cell of the body-centered orthorhombic $CeCu_2$ type structure contains only six atoms. This small number of atoms allows calculations of the interatomic forces with an accuracy high enough for obtaining correct phonon energies and eigenvectors. For calculating the whole phonon dispersion relation of a metallic compound it is necessary to take large supercells with many atoms (for a description of the method see, e.g., Eichler et al. [19]). This would require an extreme computational effort in the case of YCu_2 because we have to treat 11 electrons per Cu atom ($3d^{10}4s^1$) and nine electrons per Y atom ($4p^6 5s^2 4d^1$) as valence electrons in the electronic band-structure calculations. Therefore the ab initio calculations were restricted to the phonons at the Γ-point. The thus obtained eigenvectors served together with the neutron and Raman data as input for the Born–von Karman fitting procedure (see Section 3.2). The calculated ab initio frequencies are shown in Fig. 4 in the [ζ00] diagram. As can be seen the agreement between the

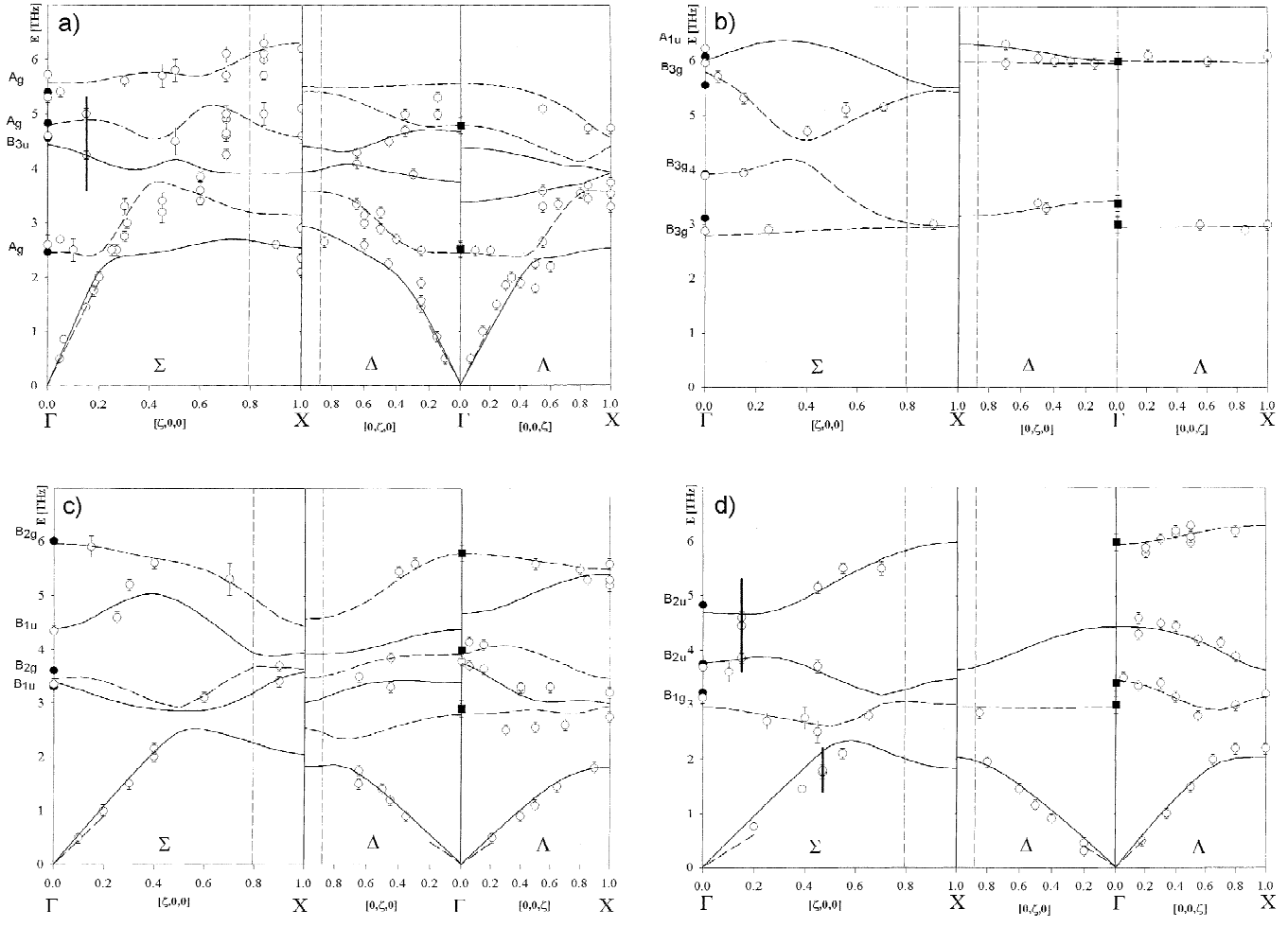

Fig. 4. Phonon dispersion relation of YCu_2. The four figures (a)–(d) correspond to the four representations expected in the three main symmetry directions (see Table 2). The open circles indicate the data points obtained by inelastic neutron scattering. The lines (full, Raman inactive; broken, Raman active) are the result of the Born–von Karman model calculation. Vertical broken lines mark the BZ-boundaries. The broken lines in the diagram (a), (c) and (d) beginning at the origin represent measurements of the elastic constants [22]. The results of the ab initio calculation are given by full circles, and the Raman data by full squares (for clarity the ab initio and the Raman data are shown separately). The vertical lines in the $[\zeta 00]$ diagrams (a) and (d) at $\zeta = 0.15$ (energy range 3.6–5.3 THz) and $\zeta = 0.47$ (energy range 1.4–2.2 THz) indicate the coordinates of the constant Q-scans as presented in Fig. 3.

Table 8
Columns from left to right: bonding between the different Cu–Cu, Y–Cu and Y–Y atoms taken into account in the Born–von Karman model

Bond type	Spring no.	Length (Å)	Long. (N/m)	Trans. (N/m)
Cu_1–Cu_2	19/20	2.47	28.3	−0.3
Cu_1–Cu_3	17/18	2.51	38.5	−1.0
Cu_1–Cu_4	15/16	2.73	14.0	1.5
Y_1–Cu_2	13/14	2.97	21.7	2.0
Y_1–Cu_2	11/12	2.98	19.7	−2.0
Y_1–Cu_1	9/10	3.11	14.7	−2.8
Y_1–Cu_1	7/8	3.12	9.3	0.1
Y_1–Y_2	5/6	3.51	28.9	−3.2
Y_1–Y_2	3/4	3.68	18.3	−3.0
Y_1–Y_1	1/2	4.31	11.4	−2.1

A numbering of the springs indicated in Fig. 1 (odd numbers correspond to longitudinal, even numbers to transversal force constants); bonding length (length of the springs); longitudinal and transversal force constants. The arrangement is made according to increasing bonding length.

ab initio eigenfrequencies and the experimentally determined eigenfrequencies is very good.

4. Comparison with other results

The lattice dynamics of YCu_2 presented above is now compared to measurements of physical properties connected with the lattice dynamics. First, we compare the calculated phonon density of states (PDOS) derived from the Born–von Karman fit and the measured PDOS. The contribution of the lattice dynamics to the specific heat is another subject. Finally thermal expansion and compressibility measurements of YCu_2 are presented and it is discussed how far the lattice dynamics reflects the anisotropy observed in the thermal expansion and compressibility.

4.1. Phonon density of states

The knowledge of the phonon density of states (PDOS)

$$g(\omega) = \sum_j \frac{1}{V_{BZ}} \int_{BZ} \mathrm{d}^3 q \; \delta(\omega - \omega_j(\vec{q})) \tag{1}$$

is of interest because the experimentally measured PDOS is a valuable proof for the Born–von Karman model fitted to the dispersion relation. Therefore the PDOS on a powdered YCu_2 sample material has been measured with a time-of-flight (TOF) spectrometer. These data have been corrected for the different scattering cross-sections in the various shells of Brillouin zones with $|\vec{Q}| = const$ (see Fig. 5). The low energy data points are not included in Fig. 5 because of contamination by the elastic line as well as incoherent scattering contributions.

One difficulty in the comparison of the measured data with the calculation arises from the fact, that the neutron scattering cross-section depends on the scattering geometry. Therefore it is necessary to compare the measurement with the calculated neutron weighted PDOS. The neutron weighted PDOS ($\bar{g}(\omega)$) and the PDOS ($g(\omega)$) are slightly different from each other. This is mainly due to the fact, that the partial contributions of Y and Cu (thin dashed and solid lines in Fig. 5) to the neutron weighted PDOS scale according to $\sqrt{b_i/M_i}$ (i=Y or Cu), where b_i and M_i is the coherent scattering length and the mass of atom i respectively.

It follows an outline of the calculation of $\bar{g}(\omega)$. The coherent inelastic scattering cross-section is given by [20]:

$$\left(\frac{\mathrm{d}^2\sigma}{\mathrm{d}\Omega\,\mathrm{d}\omega}\right)_{\mathrm{coh}}^{\mathrm{inel}} = \frac{k_f}{k_i}\frac{(2\pi)^3}{V}\sum_{\vec{\tau}}\sum_{j\,\vec{q}} \delta(\vec{Q} + \vec{q} - \vec{\tau})|H_{\vec{q}}^{j}(\vec{Q})|^2 S_j \tag{2}$$

$$S_j = \frac{1}{2\omega_j}\{(1+n_j)\delta(\omega - \omega_j(\vec{q})) + (n_j)\delta(\omega + \omega_j(\vec{q}))\} \tag{3}$$

$$H_{\vec{q}}^{j}(\vec{Q}) = \sum_d \frac{\bar{b}_d}{\sqrt{M_d}} \mathrm{e}^{-w_d + i\vec{Q}\cdot\vec{d}}\{\vec{Q}\cdot\vec{u}_d^{\,j}\} \tag{4}$$

where the coherent scattering length of the atom at position $\vec{d}$ is denoted by $\bar{b}_d$. The different phonon-branches at wave vector $\vec{q} \in BZ$ are enumerated by the running index j. The polarization vector of a phonon enters via $\vec{u}_d^{\,j}$. The thermal population of the phonons is given by n_j. The vector $\vec{Q} = \vec{k}_i - \vec{k}_f$ is the scattering vector and $\Sigma_{\vec{\tau}}$ runs over all reciprocal lattice vectors $\vec{\tau}$.

When summing up all scattering vectors $\vec{Q}$ allowed by the geometric conditions during the scattering experiment, one can calculate the neutron weighted coherent density of states:

$$\bar{g}(\omega) = \sum_{\vec{Q}} \frac{\omega}{Q^2}\left(\frac{\mathrm{d}^2\sigma}{\mathrm{d}\Omega\,\mathrm{d}\omega}\right)_{\mathrm{coh}}^{\mathrm{inel}} \tag{5}$$

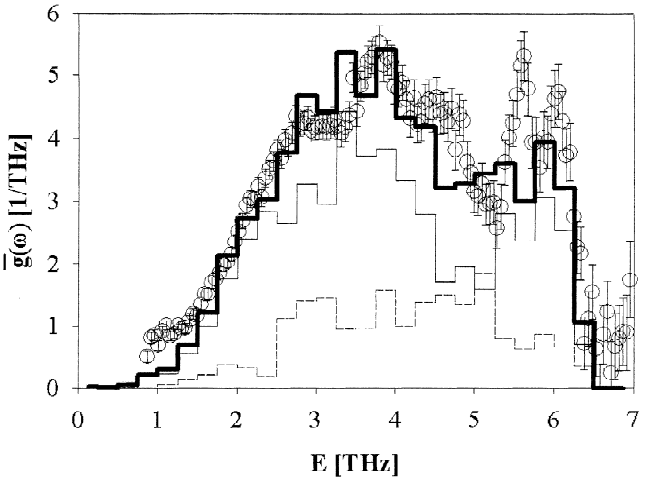

Fig. 5. Neutron weighted phonon density of states of YCu_2. The symbols are the experimental data from neutron experiments using a time-of-flight spectrometer. The histogram (thick line) is the result of the neutron weighted PDOS calculation based on the Born–von Karman model. The thin dashed and solid lines show the Y- and Cu-contribution to the PDOS, respectively.

The partial PDOS can be calculated summing only the Cu or Y atoms in Eq. (4).

As it can be seen in Fig. 5, the general feature of the measured PDOS is correctly reproduced by the calculation.

4.2. Specific heat

If the PDOS is known, the lattice specific heat per mole can be calculated using the formula

$$C_v(T) = 3R\int \mathrm{d}\omega \left(\frac{\hbar\omega}{2k_{\mathrm{B}}T}\right)^2 \sinh^{-2}\left(\frac{\hbar\omega}{2k_{\mathrm{B}}T}\right)\; g(\omega) \tag{6}$$

In order to show whether the lattice specific heat can be correctly described in the scope of the Born–von Karman model, the PDOS ($g(\omega)$) obtained from this model was used to calculate the lattice specific heat. The agreement between the measurement and the calculation (including the electronic contribution—see below) is shown in Fig. 6 in a C/T versus T representation. The C/T versus T^2-diagram of the insert depicts the determination of the electronic specific heat from the data. The γ-value of the electronic specific heat contribution (γT) has been found to be $\gamma = 8.9$ mJ/(mol K^2). The broken line in the insert represents the calculated phonon contribution in the lowest temperature range up to 10 K.

4.3. Elastic constants

From the initial slope of the acoustic phonon branches in the three main symmetry directions, the c_{ii} components ($i = 1 \ldots 6$) of the elastic tensor c_{ij} can be determined (where the compressed matrix notation for the elastic

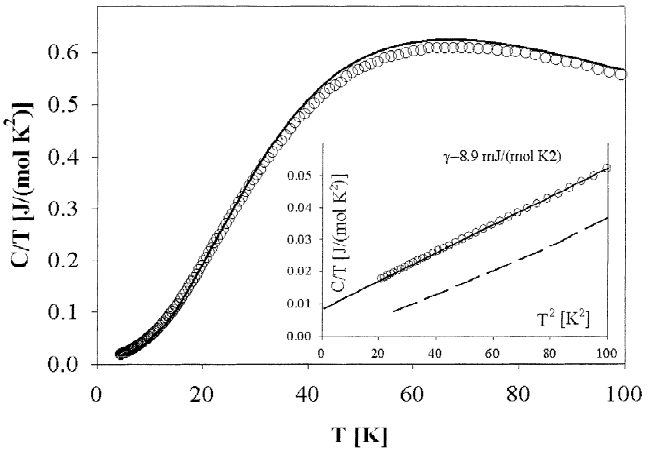

Fig. 6. Specific heat of YCu_2 in a C/T versus T plot (main frame). The experimental data are given by the symbols. The full line represents the calculated lattice specific heat together with the experimentally determined electronic part. Insert: the electronic specific heat has been determined from an extrapolation in a C/T versus T^2 plot (solid line). The broken line shows the pure lattice specific heat.

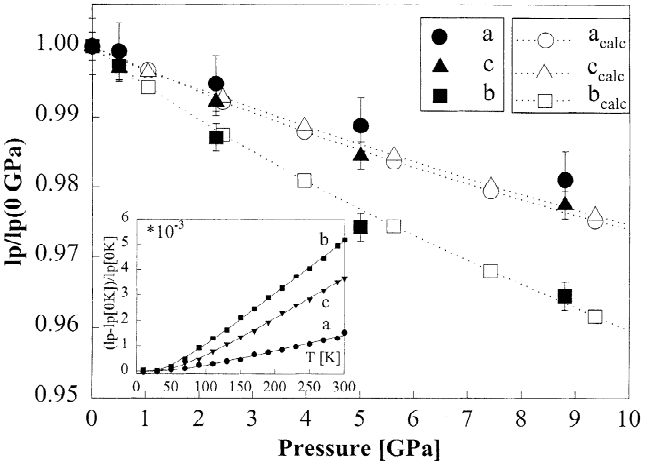

Fig. 7. The full symbols in the main frame show the normalized experimentally determined pressure dependence of the lattice parameters (lp) for YCu_2 [10]. The open symbols are the results of ab initio calculations [10]. Insert: thermal expansion in *a*, *b* and *c* direction normalized to 0 K. The full lines depict a Debye model fit.

tensor introduced by Nye [21] has been used). Because the initial slope of the three acoustic phonon branches were measured in the three main symmetry directions the components c_{ii} ($i = 4,5,6$) are obtained twice (e.g., c_{44} can be obtained from the transversal acoustic phonons with $\vec{q} = (0\zeta 0)$ and polarization in *c*-direction, as well as from the transversal acoustic phonons with $\vec{q} = (00\zeta)$ and polarization in *b*-direction). All obtained values of c_{ii} are given in the lower part of Table 9. Due to the experimental uncertainties, the double defined c_{ii} values show two different values. In the upper part of this table, elastic constants obtained from ultrasonic measurements [22] and from the Born–von Karman model calculation are given. Taking into account the uncertainties in the experiments and in the model calculation the agreement in the general tendency is satisfying. The biggest deviation is observed for c_{33}, due to the big slope of the corresponding longitudinal acoustic branch (see the $[00\zeta]$ diagram in Fig. 4a).

Table 9
Elastic constants from ultrasonic measurements done by Settai et al. [22], from the Born–von Karman model calculation and from the neutron scattering experiments are compared

Ultrasonic data (10^{11} erg/cm^3)			
c_{11}, c_{66}, c_{55}	11.4	–	–
c_{66}, c_{22}, c_{44}	1.11	9.6	–
c_{55}, c_{44}, c_{33}	2.48	1.38	10.8
Born–von Karman model (10^{11} erg/cm^3)			
c_{11}, c_{66}, c_{55}	12.1	–	–
c_{66}, c_{22}, c_{44}	1.74	9.35	–
c_{55}, c_{44}, c_{33}	3.23	1.97	9.5
Neutron data (10^{11} erg/cm^3)			
c_{11}, c_{66}, c_{55}	12.1	1.59	3.07
c_{66}, c_{22}, c_{44}	1.11	7.9	1.26
c_{55}, c_{44}, c_{33}	2.57	1.86	12.2

4.4. Thermal expansion and compressibility

The thermal expansion at ambient pressure was measured by X-ray diffraction (insert in Fig. 7) using a Siemens D500 diffractometer equipped with a helium flow cryostat. From these data, the Debye temperatures $\Theta_{D,i}$ for the different crystallographic directions $i = a,b,c$, as well as $\Theta_{D,V}$ for the volume expansion, were determined by fitting Debye integrals to the experimental data. The corresponding Debye temperatures were also determined from the slope of the acoustic phonon branches. A Debye wave-vector $q_D = 1.488$ Å^{-1} was used. The Debye temperature for each direction is obtained by averaging the Debye temperatures of the three acoustic phonon branches. The results obtained from thermal expansion and neutron scattering are given in Table 10. In both cases, the highest Θ_D value is found in the *a*-direction, whereas the *b*-direction shows the lowest Debye temperature. The higher values obtained by neutron diffraction stem from an overestimation of the highest phonon energies (for the simplest linear chain, there is an overestimation of $\pi/2$).

The fact that $\Theta_{D,b}$ is significantly smaller than $\Theta_{D,a}$ and

Table 10
Debye temperatures obtained from the slope of the acoustic phonon branches and thermal expansion

	$\Theta_{D,a}$ (K)	$\Theta_{D,b}$ (K)	$\Theta_{D,c}$ (K)	$\Theta_{D,V}$ (K)
Neutron scattering	320	274	312	–
Thermal expansion	239±40	168±12	225±12	197±9

$\Theta_{D,c}$ is in agreement with the higher compressibility in *b*-direction as shown in the main frame of Fig. 7.

5. Conclusion

In order to study the lattice dynamics of the orthorhombic YCu_2 compound inelastic neutron scattering experiments were performed and an axially symmetric Born–von Karman spring model was fitted to the experimental data. Additional information for the Born–von Karman fit was gained from ab initio calculations of the lattice dynamics at the Γ-point and from Raman measurements. It was found that for a satisfying fit of the neutron data at least 10 springs (with altogether 20 force constants) are required. A comparison of the calculated PDOS (from the Born–von Karman fit) and the measured PDOS (from a time-of-flight experiment) shows good agreement. Other confirmations of the reliability of the fit procedure and the presented lattice dynamics of this low symmetric compound have been obtained by considering specific heat, elastic constants, thermal expansion and compressibility data. All these facts provide a consistent picture of the lattice dynamics of YCu_2. A comparison with the 1:2 Y-containing Laves phases (i.e., YAl_2, YFe_2) [14,15] shows that owing to the structural change from the cubic Laves phase to the orthorhombic $CeCu_2$-type structure a significant softening of the lattice takes place. It is obvious that the anisotropy observed in many of the physical properties in the whole family of the RCu_2 compounds is closely related to the lattice dynamics in these compounds. The now available knowledge of the lattice dynamics in YCu_2 is essential for our present investigation of the phonon–crystal field interaction in $NdCu_2$. Strong evidences for this kind of interaction have been found in a number of preliminary experiments.

Acknowledgements

A.L. wishes to thank the Austrian Academy of Sciences (APART 10739) and the Austrian Science Fund (P14932).

References

[1] E. Burzo, A. Chelkoviski, H.K. Kirchmayr, in: H.P.J. Wijn (Ed.), Numerical Data and Fundamental Relationship in Science and Technology, Landoldt-Börnstein, Vol. 19, subvol. d2, Springer, Berlin, 1990, p. 1.
[2] M. Loewenhaupt, T. Reif, P. Svoboda, S. Wagner, M. Waffenschmidt, H. v Loehneysen, E. Gratz, M. Rotter, B. Lebech, T. Hauss, Z. Phys. B 101 (1996) 499.
[3] M. Rotter, M. Loewenhaupt, S. Kramp, N.M. Pyka, W. Schmidt, R. Kamp, Eur. Phys. J. B 14 (2000) 29.
[4] E. Gratz, in: Encyclopedia of Materials: Science and Technology, Elsevier, Amsterdam, 2001, p. 4152.
[5] E. Gratz, A. Lindbaum, J. Magn. Magn. Mater. 137 (1994) 115.
[6] E. Gratz, M.J. Zuckermann, in: K.A. Gscheidner, L. Eyring (Eds.), Handbook of the Physics and the Chemistry of the Rare Earth, Vol. 5, North Holland, Amsterdam, 1982, p. 117.
[7] http://www.fz-juelich.de/iff/Institute/ins/Broschuere_NSE/unidas.shtml
[8] http://houdini.pns.anl.gov/ipns/LRMECS.htm
[9] P. Knoll, R. Singer, W. Kiefer, Appl. Spectrosc. 44 (1990) 776.
[10] A. Lindbaum, J. Hafner, E. Gratz, B. Heathman, J. Phys.: Condensed Matter 10 (1998) 2933.
[11] G. Burns, in: Introduction to Group Theory with Applications, Academic Press, London, 1977, p. 385.
[12] G. Eckold, UNISOFT user manual KFA-Jülich GmbH; Jül-Spez-366 (1992).
[13] H.R. Schober, W. Petry, in: V. Gerold (Ed.), Materials Science and Technology, Vol. 1, VCH, Weinheim, New York, Basel, Cambridge, 1993, p. 289.
[14] C.T. Yeh, W. Reichardt, B. Renker, N. Nücker, M. Loewenhaupt, J. Phys. C6 (12) (1981) C6–371.
[15] L. Paolasini, B. Hennion, A. Panchula, K. Myers, P. Canfield, Phys. Rev. B 58 (1998) 12125.
[16] G. Kresse, J. Hafner, Phys. Rev. B 48 (1993) 13115.
[17] G. Kresse, J. Furthmueller, Comput. Mater. Sci. 6 (1996) 15.
[18] G. Kresse, J. Furthmueller, Phys. Rev. B 54 (1996) 11169.
[19] A. Eichler, K.-P. Bohnen, W. Reichardt, J. Hafner, Phys. Rev. B 57 (1998) 324.
[20] S.W. Lovsey, in: Theory of Neutron Scattering by Condensed Matter, Vol. I, Oxford Science Publications/Clarendon Press, Oxford, 1984.
[21] F. Nye, in: Physical Properties of Crystals, Oxford Science Publications/Clarendon Press, Oxford, 1985.
[22] R. Settai, T. Goto, Y. Onuk, J. Phys. Soc. Jpn. 61 (1992) 609.